

Article

Selective CO₂ Fixation to Styrene Oxide by Ta-Substitution of Lindqvist-Type [(Ta,Nb)₆O₁₉]⁸⁻ Clusters

Vorakit Chudatemiya ¹, Mio Tsukada ¹, Hiroki Nagakari ¹, Soichi Kikkawa ^{1,2}, Jun Hirayama ^{1,2}, Naoki Nakatani ¹, Takafumi Yamamoto ³ and Seiji Yamazoe ^{1,2,4,*}

¹ Department of Chemistry, Graduate School of Science, Tokyo Metropolitan University, 1-1 Minami-Osawa, Hachioji 192-0397, Tokyo, Japan

² Elements Strategy Initiative for Catalysts & Batteries (ESICB), Kyoto University, 1-30 Goryo-Ohara, Nishikyo-ku, Kyoto 615-8245, Japan

³ Laboratory for Materials and Structures, Tokyo Institute of Technology, 4259 Nagatsuta-cho, Midori-ku, Yokohama 226-8503, Kanagawa, Japan

⁴ Precursory Research for Embryonic Science and Technology (PRESTO), Japan Science and Technology Agency (JST), Tokyo 102-0076, Japan

* Correspondence: yamazoe@tmu.ac.jp

Abstract: Metal oxide clusters composed of group 5 metal ions, such as Nb and Ta, exhibit catalytic activities for CO₂ fixation to styrene oxide (SO) due to the highly negative natural bonding charge of the terminal O atoms that could work as CO₂ activation sites. In this study, tetrabutylammonium (TBA) salts of [Ta_xNb_{6-x}O₁₉]⁸⁻ (TBA-Ta_xNb_{6-x}, x = 0–6) were prepared and Ta-substitution effect on the catalytic properties of TBA-Ta_xNb_{6-x} for CO₂ fixation to SO was investigated. We found that TBA-Ta₁Nb₅ shows the highest styrene carbonate (SC) selectivity (95%) among TBA-Ta_xNb_{6-x}, although the SO conversion monotonously increases with the incremental Ta substitution amount. The CO₂ fixation to SO under various conditions and in situ X-ray absorption fine structure measurements reveal that CO₂ is activated on both terminal O sites coordinated to the Ta (terminal O_{Ta}) and Nb (terminal O_{Nb}) sites, whereas the activation of SO proceeds on the terminal O_{Ta} and/or bridge O sites that are connected to Ta. Density functional theory (DFT) calculations reveal that the terminal O_{Ta} of TBA-Ta₁Nb₅ preferentially adsorbs CO₂ compared with other O_{Nb} base sites. We conclude that the selective CO₂ activation at terminal O_{Ta} of TBA-Ta₁Nb₅ without SO activation is a crucial factor for high SC selectivity in the CO₂ fixation to SO.

Keywords: mixed metal oxide clusters; CO₂ fixation; base catalyst; polyoxometalate; Nb; Ta



Citation: Chudatemiya, V.; Tsukada, M.; Nagakari, H.; Kikkawa, S.; Hirayama, J.; Nakatani, N.; Yamamoto, T.; Yamazoe, S. Selective CO₂ Fixation to Styrene Oxide by Ta-Substitution of Lindqvist-Type [(Ta,Nb)₆O₁₉]⁸⁻ Clusters. *Catalysts* **2023**, *13*, 442. <https://doi.org/10.3390/catal13020442>

Academic Editor: Oxana Kholdeeva

Received: 30 December 2022

Revised: 15 February 2023

Accepted: 16 February 2023

Published: 18 February 2023



Copyright: © 2023 by the authors. Licensee MDPI, Basel, Switzerland. This article is an open access article distributed under the terms and conditions of the Creative Commons Attribution (CC BY) license (<https://creativecommons.org/licenses/by/4.0/>).

1. Introduction

Several CO₂ usage approaches have been implemented to reduce the impact of emitted greenhouse gases and to achieve a carbon neutral level. CO₂ utilization in chemical production gained significant attention in replacing traditionally used C1 sources such as phosgene or CO, which pose more toxicity. However, the activation of CO₂ is challenging due to its thermodynamic stability, which requires appropriate catalysts, such as solid base catalysts, for instance, alkaline earth metal oxides. One of the useful reactions is CO₂ cycloaddition to epoxides, which form cyclic carbonates. The resultant cyclic carbonates could be applied as solvents [1–5], monomers [6–9], electrolytes [10–13], and pharmaceuticals [14,15].

Recent applications of metal oxide clusters, namely, polyoxometalates, as base catalysts have been reported [16–22]. One of the advantages of utilizing metal oxide clusters over bulk solid base catalysts is that it does not require the surface activation of catalysts [23]. Up to now, the basicity of metal oxide clusters depends on the structures and the type of metal ions. The Lindqvist-type polyoxotungstate [W₆O₁₉]²⁻ shows the basicity with pK_a value of 11.1 and defective Keggin-type Ge-incorporated polyoxotungstate [γ-H₂GeW₁₀O₃₆]⁶⁻

exhibits high basicity with a pK_a value of 21.9 [24]. The series of group 5 metal polyoxometalates exhibit superior basicity to those of group 6 metal polyoxometalates, and the basicities of $[\text{Nb}_{10}\text{O}_{28}]^{6-}$, $[\text{Nb}_6\text{O}_{19}]^{8-}$, and $[\text{Ta}_6\text{O}_{19}]^{8-}$ increase to a pK_a value of 23.8 [17,18]. Recently, Uchida's group reported that porous ionic crystals containing Nb/Ta were applied to Knoevenagel condensation reactions as base catalyst [19]. Density functional theory (DFT) calculations reveal that the base strength of the clusters is related to the natural bond orbital (NBO) charges of the surface O atoms and the higher negativity of the NBO charges leads to stronger basicity [16,18]. We reported that Lindqvist-type polyoxometalates with group 5 metal ions (Nb, Ta) had higher negative NBO charges compared to group 6 metal ions (Mo, W) and $[\text{Nb}_6\text{O}_{19}]^{8-}$ and $[\text{Ta}_6\text{O}_{19}]^{8-}$ could activate CO_2 and worked as catalysts for CO_2 fixation and conversion reactions [18,25]. The CO_2 was activated on the terminal O sites of metal oxide clusters, which are Lewis base sites, and activated CO_2 reacts with epoxides to form carbonates [17,18,21]. The cycloaddition of CO_2 to epichlorohydrin proceeded on Keggin-type $\text{Na}_{16}[\text{SiNb}_{12}\text{O}_{40}]$ [21]. In the case of Lindqvist-type $[\text{M}_6\text{O}_{19}]^{8-}$ ($\text{M} = \text{Nb}, \text{Ta}$), $[\text{Ta}_6\text{O}_{19}]^{8-}$ showed higher activity for CO_2 fixation to styrene oxide (SO) at 403 K than $[\text{Nb}_6\text{O}_{19}]^{8-}$ [18]. However, the styrene carbonate (SC) selectivity of $[\text{Ta}_6\text{O}_{19}]^{8-}$ was lower than 90% and byproducts were formed. In our previous study, Brønsted basicity was investigated using sodium salts of $[\text{Ta}_x\text{Nb}_{6-x}\text{O}_{19}]^{8-}$ as solid base catalyst in Knoevenagel condensation reactions and local symmetry of NbO_6 and TaO_6 units in the clusters affected base catalytic properties [23]. In this study, tetrabutylammonium (TBA) salts of mixed metal oxide clusters $[\text{Ta}_x\text{Nb}_{6-x}\text{O}_{19}]^{8-}$ (TBA- $\text{Ta}_x\text{Nb}_{6-x}$, $x = 0-6$) were prepared and applied to CO_2 fixation to SO to elucidate the Ta-substitution effect on the catalytic activities and selectivity. It was found that single-Ta-substituted TBA- Ta_1Nb_5 exhibited the highest SC selectivity among TBA- $\text{Ta}_x\text{Nb}_{6-x}$. We demonstrated that the high SC selectivity was achieved by the selective adsorption of CO_2 on the terminal O_{Ta} without SO activation under reaction conditions.

2. Results

The fabricated TBA- $\text{Ta}_x\text{Nb}_{6-x}$ were characterized by X-ray absorption spectroscopy (XAS), electrospray ionization mass spectrometry (ESI-MS), Fourier-transformed infrared (FT-IR) in attenuated total reflectance (ATR) mode, and elemental analysis (Figures 1, S1 and S2, Table S1, respectively). ESI-MS suggests that the various components of Ta-Nb mixed metal oxide clusters are contained in the TBA- $\text{Ta}_x\text{Nb}_{6-x}$. Ta L_3 -edge Fourier-transformed extended X-ray absorption fine structure (FT-EXAFS) of TBA- $\text{Ta}_x\text{Nb}_{6-x}$ indicates that peaks of Ta-M ($\text{M} = \text{Nb}$ or Ta) shift to a longer length with increasing Ta content (Figure 1a). A similar peak shift of Nb-M ($\text{M} = \text{Nb}$ or Ta) is observed in the Nb K-edge FT-EXAFS spectra (Figure 1b). Those indicate the Ta-substitution to Nb sites in $[\text{Ta}_x\text{Nb}_{6-x}\text{O}_{19}]^{8-}$. Elemental analysis reveals that TBA/ $[\text{Ta}_x\text{Nb}_{6-x}\text{O}_{19}]^{8-}$ ratio is 5~6.

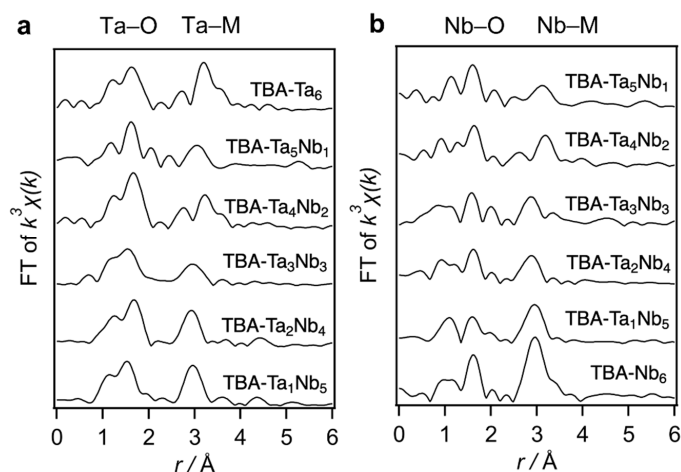


Figure 1. (a) Ta L_3 -edge and (b) Nb K-edge FT-EXAFS spectra of TBA- $\text{Ta}_x\text{Nb}_{6-x}$. The Ta-O (Nb-O) and Ta-M (Nb-M) are shown in r ranges of 1.2–2.0 Å and 2.5–3.4 Å, respectively.

The prepared clusters were employed in the catalytic CO₂ fixation to SO. Figure 2 shows the SO conversion and SC selectivity for TBA-Ta_xNb_{6-x} catalysts. The SO conversion gradually increases with incremental addition of Ta content and TBA-Ta₆ exhibits the highest SO conversion among them. On the other hand, the trend of SC selectivity for the composition of clusters differs from that of SO conversion (Figure 2). Interestingly, single-Ta-substituted TBA-Ta₁Nb₅ provides the highest SC selectivity (95%) among the mixed metal oxide clusters. Further Ta-substitution decreases SC selectivity and the SC selectivity becomes constant in Ta-rich TBA-Ta_xNb_{6-x} catalysts ($x = 4-6$). The number of TBA counteractions has a negligible impact on this reaction, although TBA/[Ta_xNb_{6-x}O₁₉]⁸⁻ ratio varies with the composition [17]. The byproducts in this reaction over TBA-Ta₆ are polymers derived from the polymerization of SO, because the SO conversion is found for TBA-Ta₆ at 100 °C under N₂ atmosphere without CO₂ despite negligible SO conversion for TBA-Nb₆, as shown in Figure S3. The high SC selectivity (95%) of TBA-Ta₁Nb₅ maintains a high SO conversion (88%) for a 24 h reaction (Figure 2). In addition, the >95% SC selectivity is only achieved by TBA-Ta₁Nb₅ among the TBA-Ta_xNb_{6-x} catalysts at >80% conversion (Figure S4). Thus, the selective CO₂ fixation to SO is achieved by the single Ta substitution to TBA-Nb₆.

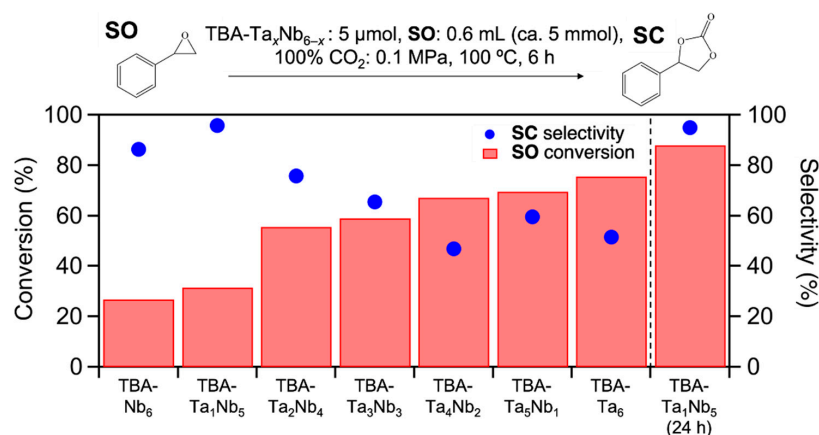


Figure 2. Results of CO₂ fixation to styrene oxide over TBA-Ta_xNb_{6-x}. Bars represent conversion of SO, blue dots represent selectivity of SC. Reaction condition: catalyst loading = 5 μmol, SO = 0.6 mL (ca. 5 mmol), 100% CO₂ = 0.1 MPa, temperature = 100 °C, reaction time = 6 h.

The time courses of CO₂ fixation to SO over TBA-Ta₆, TBA-Ta₁Nb₅, and TBA-Nb₆ are shown in Figures 3 and S5. The trends of conversion and selectivity depend on the composition of the clusters. TBA-Ta₆ exhibits the highest reaction rate among them, and SC selectivity increases with reaction time. TBA-Ta₁Nb₅ and TBA-Nb₆ show high SC selectivity at the initial stage of the reaction and the SC selectivity is maintained at a high SO conversion. Thus, TBA-Nb₆ and single-Ta-substituted TBA-Ta₁Nb₅ have the specific active sites for selective SC formation. The increment in the SC selectivity over TBA-Ta₆ is due to the consumption of SO and suppression of undesired reactions during the reaction.

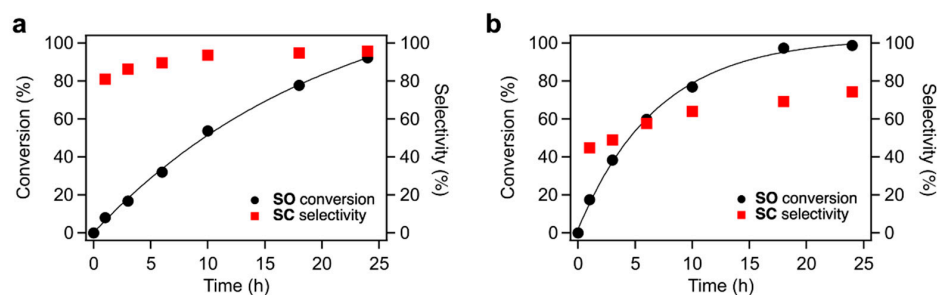


Figure 3. Time courses of SO conversion in CO₂ fixation to SO using (a) TBA-Ta₁Nb₅ and (b) TBA-Ta₆ as the catalysts. Reaction condition: catalyst loading = 10 μmol, SO = 1.2 mL (ca. 10 mmol), 100% CO₂ = 0.1 MPa, temperature = 100 °C.

Effects of **SO** concentration and CO_2 concentration on the CO_2 fixation to **SO** were studied for TBA-Ta₁Nb₅ (Figure 4). When increasing the **SO** concentration in the dimethyl sulfoxide (DMSO) solution, the **SC** selectivity slightly increases while maintaining the **SO** conversion. On the other hand, the **SC** selectivity dramatically decreases with decreasing CO_2 concentration (Figure 4b), suggesting the CO_2 activation is a key step in the CO_2 fixation to **SO**. We reported that CO_2 fixation to **SO** proceeds due to the fact that the CO_2 is activated on the terminal O sites and activated CO_2 reacts with **SO** to form **SC** [17,18]. The rate determining step of CO_2 fixation to **SO** is the nucleophilic attack of activated CO_2 to **SO**. The above results could be explained by the reaction mechanism. The decrease in the **SC** yield by reducing **SO** concentration, as shown in Figure 4a, is due to the inhibition of the reaction of activated CO_2 with **SO** by a low **SO** concentration. There are two reasons for the drastic decrease in **SC** selectivity by reducing CO_2 concentration. One is the decrease in the amount of activated CO_2 . The other is that **SO** can be activated on TBA-Ta₁Nb₅ in low CO_2 concentration conditions. In fact, the **SO** conversion of TBA-Ta₁Nb₅ under N_2 atmosphere without CO_2 is higher than that of TBA-Nb₆, as shown in Figure S3, suggesting that the **SO** activation occurs by single Ta-substitution at a low CO_2 concentration.

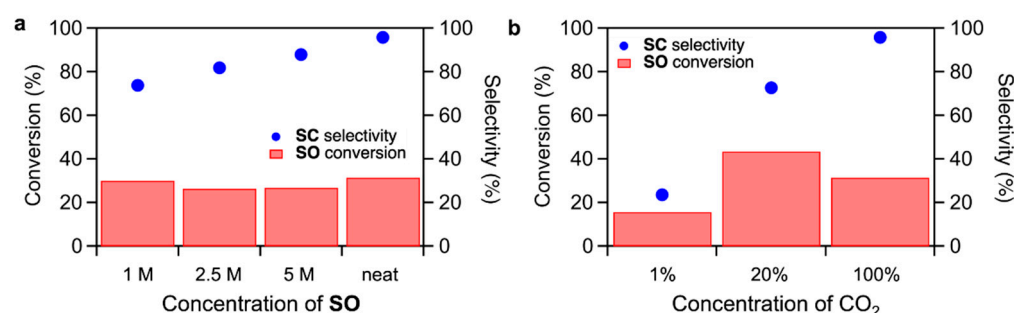


Figure 4. Effect of (a) **SO** concentration and (b) CO_2 concentration with N_2 balance. Reaction conditions: (a) TBA-Ta₁Nb₅ = 5 μmol , DMSO = 1 mL, **SO** = 0.6 mL (ca. 5 mmol for neat condition), 100% CO_2 = 0.1 MPa, temperature = 100 $^\circ\text{C}$, reaction time = 6 h; (b) TBA-Ta₁Nb₅ = 5 μmol , **SO** = 0.6 mL (ca. 5 mmol), neat, CO_2 (0.1 MPa), temperature = 100 $^\circ\text{C}$, reaction time = 6 h.

3. Discussion

We reported that the CO_2 fixation to **SO** proceeded on the terminal O sites of TBA-Ta₆ because the terminal O sites, which have the negatively charged O, work as Lewis base sites [18]. The CO_2 is activated on the terminal O sites and the activated CO_2 reacts with **SO** to form **SC**. The CO_2 adsorption on TBA-Nb₆, TBA-Ta₁Nb₅, and TBA-Ta₆ in **SO** was examined by in situ XAFS measurements (Figure 5). Nb K-edge XANES spectrum of TBA-Nb₆ in **SO** exhibits a pre-edge peak at 18,980.5 eV assigned to electron excitation from 1s to hybridized 4d–5p [26,27]. This pre-edge peak intensity gives us the information on the distortion from NbO₆ octahedral (*Oh*) symmetry. The pre-edge peak intensity decreases with the CO_2 introduction to TBA-Nb₆ in **SO**, which indicates that the *Oh* symmetry of NbO₆ in TBA-Nb₆ is improved by the CO_2 addition. Similar results were obtained for TBA-Ta₁Nb₅, as shown in Figure 5b. Ta L₁-edge XANES spectra indicate that the pre-edge peak at 11,686 eV, which is assigned to electron transition from Ta 2s orbitals to hybridized 5d–6p orbitals [26,27], decreases with the introduction of CO_2 . This change of pre-edge peak intensity reveals that TaO₆ *Oh* symmetry is also improved by the CO_2 addition to TBA-Ta₆ and TBA-Ta₁Nb₅. These results suggest that the *Oh* symmetry of TaO₆ unit increases, while NbO₆ symmetry is slightly improved in TBA-Ta₁Nb₅ by CO_2 adsorption. Actually, the optimized structure of [Ta₁Nb₅O₁₉]⁸⁻ with CO_2 adsorbed on the terminal O_{Ta} site has highly *Oh* symmetric TaO₆ units compared to the bare [Ta₁Nb₅O₁₉]⁸⁻ (Figure S6) CO_2 is also adsorbed on TBA-Ta_xNb_{6-x} in **SO** solution. This structural change induced by CO_2 adsorption is also observed in FT-IR (Figure S7). FT-IR spectra of TBA-Ta₁Nb₅ in DMSO solvent show the characteristic absorption band assignable to the stretching vibration between the metal and terminal O atoms in MO₆ units (M=O bond). The absorption band

shifts to high energy, owing to the slight shrink in the O=Nb bond in NbO₆ units. Those results indicate that CO₂ is preferentially adsorbed on terminal O sites of TaO₆ unit and induces the structure change in TBA-Ta_xNb_{6-x}.

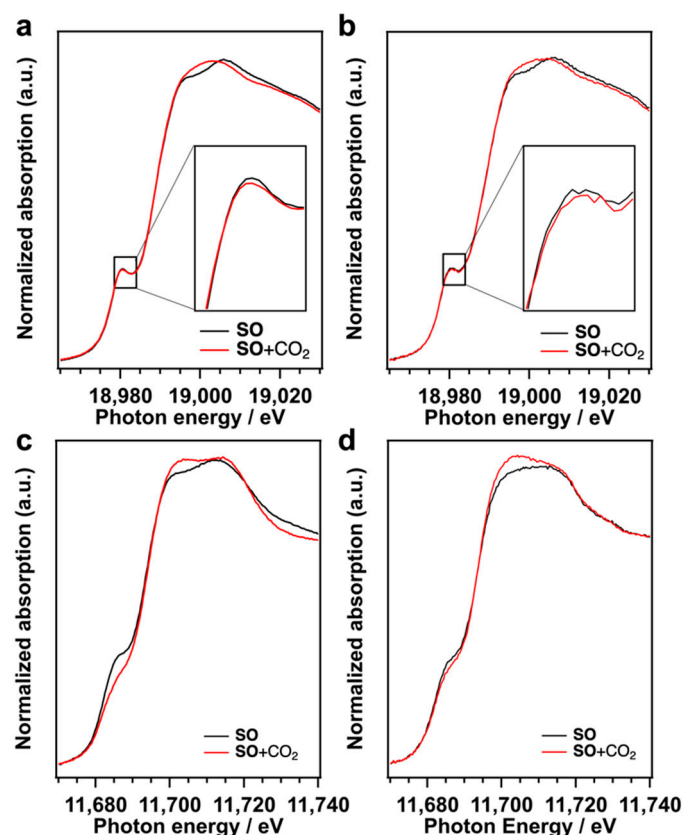


Figure 5. (a) Nb K-edge of TBA-Nb₆ and (b) TBA-Ta₁Nb₅, and (c) Ta L₁-edge XANES spectra of TBA-Ta₆ and (d) TBA-Ta₁Nb₅ in SO solution before (black line) and after (red line) introduction of CO₂.

Next, NBO charges of the surface O atoms of TBA-Ta_xNb_{6-x} were calculated to elucidate the catalytic activity and selectivity of TBA-Ta_xNb_{6-x} for CO₂ fixation to SO (Figure 6). The average NBO charge was also evaluated in Figure 6. The terminal O atoms coordinated to Ta (terminal O_{Ta}) have the most negative NBO charges (highest basicity) followed by the bridge O atom between Ta ions (bridge O_{Ta-Ta}) in TBA-Ta_xNb_{6-x}. The values of NBO charge of terminal O_{Ta} hardly change with the Ta content. On the other hand, the NBO charge of the terminal O connecting to Nb (terminal O_{Nb}) has lower negativity than that of terminal O_{Ta}. The order of NBO charges in TBA-Ta_xNb_{6-x} is terminal O_{Ta}, bridge O_{Ta-Ta}, bridge O_{Ta-Nb} (Ta–O–Nb), terminal O_{Nb}, and bridge O_{Nb-Nb} (Nb–O–Nb). As a result, the average NBO charges of TBA-Ta_xNb_{6-x} gradually increase with increasing the Ta content. The catalytic activities of TBA-Ta_xNb_{6-x}, which increase with incremental addition of Ta content in Figure 2, could be explained by the average NBO charges, indicating the increase in the active sites of terminal O_{Ta} by Ta substitution.

Finally, the CO₂ adsorption sites of [Ta₁Nb₅O₁₉]⁸⁻ were also predicted by DFT calculations. We reported that CO₂ was preferentially adsorbed on terminal O sites rather than bridge O sites [18]. [Ta₁Nb₅O₁₉]⁸⁻ has three terminal O sites (see Figure 7). To determine the CO₂ activation sites of [Ta₁Nb₅O₁₉]⁸⁻, the CO₂ adsorption energy was calculated using three possible configurations (Figure 7). Among the three structures, the lowest energy is found in a structure with CO₂ adsorbed on the terminal O_{Ta} site, which has the highest negative NBO charge among the surface oxygen atoms in [Ta₁Nb₅O₁₉]⁸⁻. This result indicates that the CO₂ is preferentially adsorbed and activated on the terminal O_{Ta}. The SO adsorption energy was also calculated to gain the insight into SO activation sites (Figure S8). The

adsorption energy of SO on O_{Ta} is lower than that of CO_2 on O_{Ta} in $[\text{Ta}_1\text{Nb}_5\text{O}_{19}]^{8-}$. In addition, adsorption energies reveal that SO is more likely to be activated on O_{Ta} than O_{Nb} . These results suggest that CO_2 preferentially adsorbs on O_{Ta} site and it is unlikely that SO activation occurs on O_{Nb} in TBA- Ta_1Nb_5 . Therefore, high SC selectivity is achieved in TBA- Ta_1Nb_5 . The low SC selectivity in Ta-rich TBA- $\text{Ta}_x\text{Nb}_{6-x}$ is explained that not only by the fact that CO_2 but also SO is activated on O_{Ta} sites by competitive adsorption due to the large number of O_{Ta} adsorption sites.

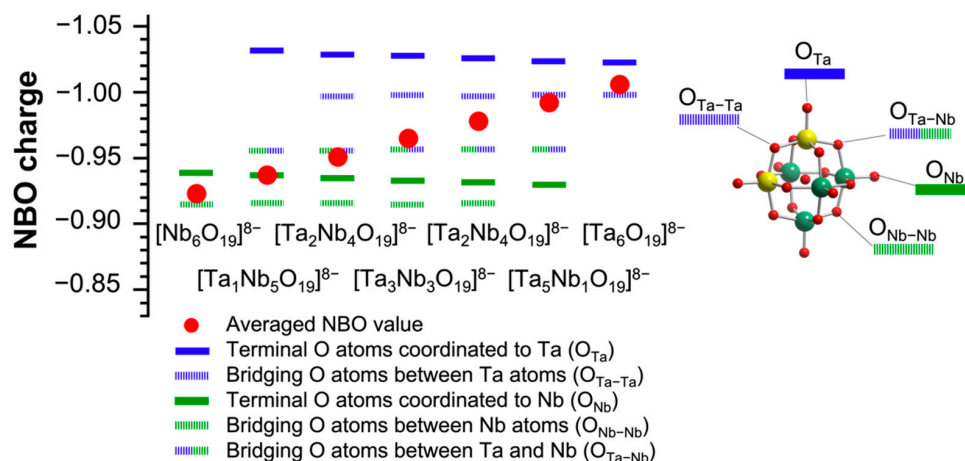


Figure 6. NBO charge of surface O sites of $[\text{Ta}_x\text{Nb}_{6-x}\text{O}_{19}]^{8-}$. Color codes: yellow atom, Ta; green atom, Nb; blue line, Ta-coordinated O atoms; green line, Nb-coordinated O atoms; red, total O atoms. Red circle represents the averaged value. Terminal and bridging O atoms represent solid and dashed lines, respectively.

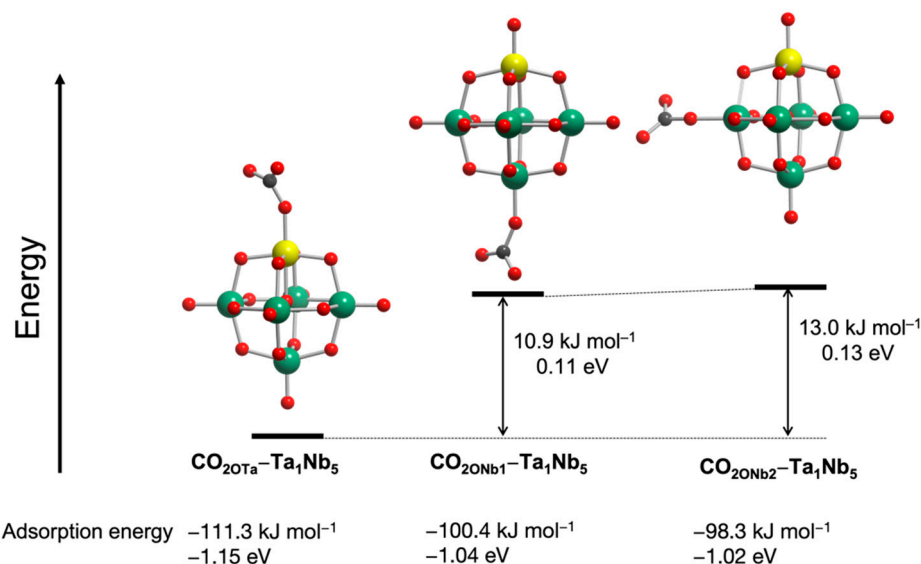
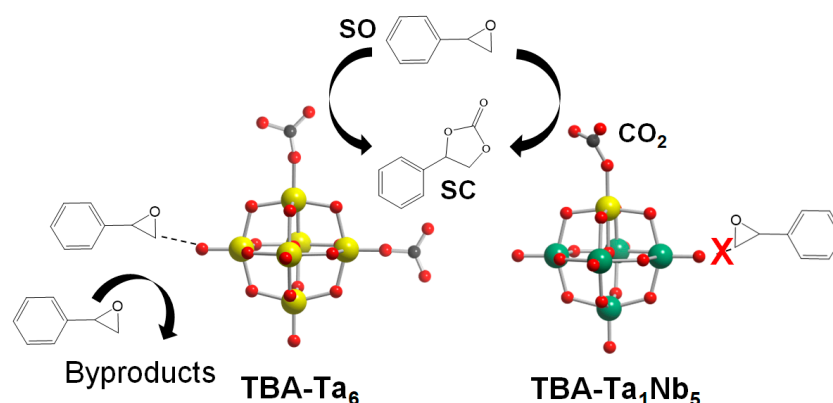


Figure 7. Total energy of CO_2 -adsorbed $[\text{Ta}_1\text{Nb}_5\text{O}_{19}]^{8-}$ at different base sites.

The reaction mechanism of TBA- $\text{Ta}_x\text{Nb}_{6-x}$ for CO_2 fixation to SO is discussed. In the case of TBA- Nb_6 , CO_2 is adsorbed on the terminal O_{Nb} sites and the activated CO_2 reacts nucleophilically with SO to form SC . The low catalytic activity of TBA- Nb_6 for CO_2 fixation to SO is due to the weak Lewis base strength (low negativity in NBO charges) of terminal O_{Nb} compared with terminal O_{Ta} of other TBA- $\text{Ta}_x\text{Nb}_{6-x}$. The SO activation hardly occurs on TBA- Nb_6 , as shown in Figure S3, which is one of the reasons why TBA- Nb_6 shows high SC selectivity. The SO conversion gradually increases with Ta substitution amount, as shown in Figure 2. This can be explained by the increase in active terminal O_{Ta} sites. On the other hand, the SC selectivity decreases for high Ta content of TBA- $\text{Ta}_x\text{Nb}_{6-x}$

($x \geq 2$). The low **SC** selectivity is due to the **SO** activation on the surface of TBA-Ta_xNb_{6-x} ($x \geq 2$), as shown in Scheme 1. In fact, TBA-Ta₆ exhibits the highest **SO** conversion among TBA-Ta₆, TBA-Ta₁Nb₅, and TBA-Nb₆ in the absence of CO₂ accompanied with a viscosity increase (Figure S3). The sharp contrast in **SO** conversion in the absence of CO₂ conditions for TBA-Ta₆ and TBA-Nb₆ clearly indicates that terminal O_{Ta} and/or bridge O_{Ta-Ta} can activate **SO**. On the other hand, TBA-Ta₁Nb₅ exhibits the highest **SC** selectivity among TBA-Ta_xNb_{6-x} despite having a terminal O_{Ta} site. The DFT calculation (Figure 7) and CO₂ concentration dependence on CO₂ fixation to **SO** (Figure 4b) reveal that the single terminal O_{Ta} in [Ta₁Nb₅O₁₉]⁸⁻ preferentially adsorbs CO₂ at 100% CO₂ conditions and **SO** is not activated on terminal O_{Nb}, bridge O_{Nb-Nb}, and bridge O_{Ta-Nb} (Scheme 1). We conclude that the selective CO₂ activation at the terminal O_{Ta} in TBA-Ta₁Nb₅ without **SO** activation is a crucial factor for high **SC** selectivity in the CO₂ fixation to **SO**.



Scheme 1. Activation of CO₂ on O_{Ta} leads to a reaction with **SO** to form **SC**, while adsorption of **SO** on O_{Ta} leads to the formation of byproducts observed in reaction promoted by TBA-Ta₆. In the case of TBA-Ta₁Nb₅, **SO** is not activated on O_{Nb} and preferential adsorption of CO₂ on O_{Ta} results in high selectivity of **SC**.

4. Materials and Methods

TBA salts of [Ta_xNb_{6-x}O₁₉]⁸⁻ (TBA-Ta_xNb_{6-x}, $x = 0-6$) were prepared by microwave-assisted hydrothermal synthesis (Biotage Initiator⁺ 400 W) using Ta_{2(x/6)}Nb_{2(1-x/6)}O₅·*n*H₂O as the precursors. First, Na₃Ta_{x/6}Nb_{1-x/6}O₄ were prepared by modified solid-state reaction method according to the reported procedures [23,28]. M₂O₅ (M = Ta or Nb), Na₂C₂O₄, and (NH₂)₂CO at a molar ratio between (Ta + Nb):Na:(NH₂)₂CO of 1:1:4 was ground to fine powder prior to calcination at 773 K for 4 h to obtain NaTa_{x/6}Nb_{1-x/6}O₃. NaTa_{x/6}Nb_{1-x/6}O₃ was mixed with Na₂C₂O₄, and (NH₂)₂CO at a molar ratio between NaTa_{x/6}Nb_{1-x/6}O₃:Na:(NH₂)₂CO of 1:1:3 followed by calcination at 1173 K for 4 h. The resulting powder, Na₃Ta_{x/6}Nb_{1-x/6}O₄, was characterized by XRD (Rigaku Miniflex) having diffraction patterns corresponding to the references (Figure S9). Na₃Ta_{x/6}Nb_{1-x/6}O₄ was dissolved in water and 1 M HCl was added until pH of the supernatant reached 1 or less. The white precipitate was collected by centrifugation and washed with pure water until the pH of the supernatant became neutral. After drying in vacuum and oven, the Ta_{2(x/6)}Nb_{2(1-x/6)}O₅·*n*H₂O was obtained. Then, 10% tetrabutylammonium hydroxide (TBAOH) aqueous solution was added to Ta_{2(x/6)}Nb_{2(1-x/6)}O₅·*n*H₂O. The mixture was reacted using microwave-assisted hydrothermal synthesis at 180 °C for 5–15 min. The resultant product was washed with hexane to obtain TBA₆H₂[Ta_xNb_{6-x}O₁₉]. The fabricated clusters were characterized by ESI-MS (Figure S1) (Bruker, MicroOTOFII-ST1), Fourier-transformed infrared spectrometry (JASCO, FT/IR-4700) equipped with attenuated total reflectance-infrared spectroscopy (JASCO, ATR-PRO ONE) (Figure S2), elemental analysis (Table S1), and X-ray absorption fine structure (XAFS) analysis (BL01B1, SPring-8) (Figure 1). XAFS spectra were recorded in transmittance mode using ionization chambers as detectors at room temperature. Si(111) double-crystal monochromator was used to

obtain the incident X-ray beam for Ta L₁- and L₃-edges XAFS. In the case of Nb K-edge XAFS measurements, Si(311) double-crystal monochromator was employed. The data were analyzed using xTunes software [29]. The XANES spectra were extracted as the extended X-ray absorption fine structure (EXAFS) after normalization at edge height. The EXAFS spectra in the *k* range 3.0–14.0 Å⁻¹ were Fourier-transformed into *r* space to obtain FT-EXAFS spectra. The illustrations of Ta_{*x*}Nb_{6-*x*}O₁₉ were computed using VESTA [30].

In general, CO₂ fixation to **SO** over TBA-Ta_{*x*}Nb_{6-*x*} were carried out using 5 μmol of catalyst, **SO** (0.6 mL, ca. 5 mmol), 100% CO₂ (0.1 MPa) at 100 °C for 6 h using biphenyl as an internal standard. The product solutions were analyzed using gas chromatography equipped with flame ionization detector (GC-FID, Shimadzu, GC-2014 with column Restex, Rtx-1) and gas chromatography–mass spectrometry (GC–MS, Shimadzu, GCMS-QP2010 SE with column Agilent, DB-1MS). Time course of CO₂ fixation to **SO** reactions were carried out using 10 μmol of catalyst, **SO** (1.2 mL, ca. 10 mmol), 100% CO₂ (0.1 MPa) at 100 °C for 24 h. Small amount of solution (ca. 20 μL) was drawn to measure at specified reaction times. The peak areas from GC-FID chromatograms were used to calculate with this formula:

$$\text{Conversion (\%)} = \left(1 - \frac{\text{Area}_{\text{Sub.}}}{\text{Area}_{\text{IS}}} \times \frac{\text{Area}_{\text{ISO}}}{\text{Area}_{\text{Sub.0}}} \right) \times 100$$

$$\text{Selectivity (\%)} = \frac{\text{Area}_{\text{Pro.}}}{\text{Area}_{\text{IS}}} \times \frac{\text{ECN}_{\text{Sub.}}}{\text{ECN}_{\text{Pro.}}} \times \frac{\text{Area}_{\text{ISO}}}{\text{Area}_{\text{Sub.0}}} \times \frac{100}{\text{Conversion (\%)}} \times 100$$

where *Sub.* = substrate (**SO**), *IS* = internal standard (biphenyl), *Pro.* = product (**SC**), *ECN* = equivalent carbon number, subscripted 0 = initial value before reaction.

The DFT calculations were conducted using Gaussian 16 program as previously reported [18]. The structural optimization for [Ta_{*x*}Nb_{6-*x*}O₁₉]⁸⁻ was performed by B3LYP with the solvation effect of DMSO using PCM (dielectric constant = 46.826). LanL2DZ basis sets were employed for Ta and Nb atoms and 6–31 + G(d) basis sets for O and C atoms to investigate the effect of the composition of the clusters on the NBO charge of O atoms and the adsorption energies of CO₂ on [Ta₁Nb₅O₁₉]⁸⁻.

5. Conclusions

In conclusion, TBA-Ta_{*x*}Nb_{6-*x*} (*x* = 0–6) were prepared by microwave-assisted hydrothermal reaction and were used as catalysts for CO₂ fixation to **SO** to produce **SC**. Among TBA-Ta_{*x*}Nb_{6-*x*}, TBA-Ta₁Nb₅ shows the highest selectivity toward **SC**, whereas the **SO** conversion increases with the Ta content in the clusters. The effects of **SO** concentration and CO₂ concentration for CO₂ fixation to **SO** indicate that high **SO** concentration and 100% CO₂ atmosphere are required to obtain high **SC** selectivity for TBA-Ta₁Nb₅ because the rate-determining step of CO₂ fixation to **SO** is the reaction of the activated CO₂ with **SO**. The **SO** conversions in the absence of CO₂ suggest that the **SO** activation hardly occurs in TBA-Nb₆. DFT calculations reveal that the increase in the **SO** conversion with Ta content is the increment of the active terminal O_{Ta} sites that have the highest negative NBO charges. In addition, [Ta₁Nb₅O₁₉]⁸⁻ preferentially adsorbs CO₂ at terminal O_{Ta} sites compared to other O_{Nb} sites. In conclusion, the selective CO₂ activation at terminal O_{Ta} in TBA-Ta₁Nb₅ without **SO** activation is a crucial factor for high **SC** selectivity in the CO₂ fixation to **SO**.

Supplementary Materials: The following supporting information can be downloaded at: <https://www.mdpi.com/article/10.3390/catal13020442/s1>, Table S1: Elemental analysis results of the synthesized TBA₆H₂[Ta_{*x*}Nb_{6-*x*}O₁₉]; Figure S1: ESI–MS (negative ion mode) spectra of TBA_{*m*}H_{*n*}[Ta_{*x*}Nb_{6-*x*}O₁₉]^{8-*m-n*} measured in aqueous solutions; Figure S2: FT-IR spectra (ATR mode) of (a) TBA-Ta₆, (b) TBA-Ta₅Nb₁, (c) TBA-Ta₄Nb₂, (d) TBA-Ta₃Nb₃, (e) TBA-Ta₂Nb₄, (f) TBA-Ta₁Nb₅, and (g) TBA-Nb₆; Figure S2: FT-IR spectra (ATR mode); Figure S3: CO₂ fixation to **SO** promoted by TBA-Ta_{*x*}Nb_{6-*x*} under N₂ atmosphere under N₂ atmosphere; Figure S4: Results of CO₂ fixation to **SO** over TBA-Ta_{*x*}Nb_{6-*x*}; Figure S5: Time course of CO₂ fixation to **SO** and selectivity of **SC** over TBA-Nb₆; Figure S6: Optimized structure of [Ta₁Nb₅O₁₉]⁸⁻ and CO₂-adsorbed [Ta₁Nb₅O₁₉]⁸⁻; Figure S7: In situ FT-IR spectra (ATR mode) of TBA-Ta₁Nb₅ in DMSO before (black line) and after CO₂ adsorption

(red line). (b) Optimized structure of $[\text{Ta}_1\text{Nb}_5\text{O}_{19}]^{8-}$ and CO_2 -adsorbed $[\text{Ta}_1\text{Nb}_5\text{O}_{19}]^{8-}$. Figure S8: Total energy of SO -adsorbed $[\text{Ta}_1\text{Nb}_5\text{O}_{19}]^{8-}$ at different base sites. Figure S9: XRD patterns of $\text{Na}_3\text{Ta}_x/6\text{Nb}_{6-x}/6\text{O}_4$.

Author Contributions: S.K. and S.Y. designed this study. V.C., M.T. and J.H. synthesized and characterized catalysts and carried out the catalytic tests. H.N. and N.N. carried out the DFT calculations and analyzed the NBO charges of the catalysts. T.Y. measured and analyzed the XRD. V.C., S.K., M.T. and S.Y. measured and analyzed the XAFS spectra. All authors have read and agreed to the published version of the manuscript.

Funding: This study was financially supported by NEDO (JPNP14004), JSPS KAKENHI (No. 20K22467, 21H01718, and 22K14543), Tokyo Human Resources Fund for City Diplomacy, Tokyo Metropolitan University Research Fund for Young Scientists, Tokyo Metropolitan Government Advanced Research (R3-1), and Yazaki Memorial Foundation for Science and Technology.

Data Availability Statement: The data that support the findings of this study are available from the corresponding author upon reasonable request.

Acknowledgments: The synchrotron radiation experiment was performed at BL01B1 in SPring-8 under the approval of the Japan Synchrotron Radiation Research Institute (JASRI) as 2020A1068, 2021B1380, 2021A1406, 2021B1535, 2022A1532, 2022A1627, 2022B1684, and 2022B1911.

Conflicts of Interest: The authors declare no conflict of interest.

References

1. North, M.; Omedes-Pujol, M. Catalytic, Asymmetric Cyanohydrin Synthesis in Propylene Carbonate. *Tetrahedron Lett.* **2009**, *50*, 4452–4454. [[CrossRef](#)]
2. Clegg, W.; Harrington, R.W.; North, M.; Pizzato, F.; Villuendas, P. Cyclic Carbonates as Sustainable Solvents for Proline-Catalysed Aldol Reactions. *Tetrahedron Asymmetry* **2010**, *21*, 1262–1271. [[CrossRef](#)]
3. Jessop, P.G. Searching for Green Solvents. *Green Chem.* **2011**, *13*, 1391. [[CrossRef](#)]
4. Forero, J.S.B.; Muñoz, J.A.H.; Junior, J.J.; Da Silva, F.M. Propylene Carbonate in Organic Synthesis: Exploring Its Potential as a Green Solvent. *Curr. Org. Synth.* **2016**, *13*, 834–846. [[CrossRef](#)]
5. Pescarmona, P.P. Cyclic Carbonates Synthesised from CO_2 : Applications, Challenges and Recent Research Trends. *Curr. Opin. Green Sustain. Chem.* **2021**, *29*, 100457. [[CrossRef](#)]
6. Fukuoka, S.; Fukawa, I.; Tojo, M.; Oonishi, K.; Hachiya, H.; Aminaka, M.; Hasegawa, K.; Komiyama, K. A Novel Non-Phosgene Process for Polycarbonate Production from CO_2 : Green and Sustainable Chemistry in Practice. *Catal. Surv. Asia* **2010**, *14*, 146–163. [[CrossRef](#)]
7. Fleischer, M.; Blattmann, H.; Mülhaupt, R. Glycerol-, Pentaerythritol- and Trimethylolpropane-Based Polyurethanes and Their Cellulose Carbonate Composites Prepared via the Non-Isocyanate Route with Catalytic Carbon Dioxide Fixation. *Green Chem.* **2013**, *15*, 934. [[CrossRef](#)]
8. Rokicki, G. Aliphatic Cyclic Carbonates and Spiroorthocarbonates as Monomers. *Prog. Polym. Sci.* **2000**, *25*, 259–342. [[CrossRef](#)]
9. Yu, W.; Maynard, E.; Chiaradia, V.; Arno, M.C.; Dove, A.P. Aliphatic Polycarbonates from Cyclic Carbonate Monomers and Their Application as Biomaterials. *Chem. Rev.* **2021**, *121*, 10865–10907. [[CrossRef](#)]
10. Zhang, S.S. A Review on Electrolyte Additives for Lithium-Ion Batteries. *J. Power Sources* **2006**, *162*, 1379–1394. [[CrossRef](#)]
11. Xu, K. Nonaqueous Liquid Electrolytes for Lithium-Based Rechargeable Batteries. *Chem. Rev.* **2004**, *104*, 4303–4418. [[CrossRef](#)]
12. Tillmann, S.D.; Isken, P.; Lex-Balducci, A. Gel Polymer Electrolyte for Lithium-Ion Batteries Comprising Cyclic Carbonate Moieties. *J. Power Sources* **2014**, *271*, 239–244. [[CrossRef](#)]
13. Yun, J.; Zhang, L.; Qu, Q.; Liu, H.; Zhang, X.; Shen, M.; Zheng, H. A Binary Cyclic Carbonates-Based Electrolyte Containing Propylene Carbonate and Trifluoropropylene Carbonate for 5V Lithium-Ion Batteries. *Electrochim. Acta* **2015**, *167*, 151–159. [[CrossRef](#)]
14. Kawai, H.; Sakamoto, F.; Taguchi, M.; Kitamura, M.; Sotomura, M.; Tsukamoto, G. 2-Oxo-1,3-Dioxoles as Specific Substrates for Measurement of Arylesterase Activity. *Chem. Pharm. Bull.* **1991**, *39*, 1422–1425. [[CrossRef](#)]
15. Cascio, G.; Manghisi, E.; Porta, R.; Fregnan, G. N-Phenylpiperazine Derivatives with Hypocholesterolemic Activity. *J. Med. Chem.* **1985**, *28*, 815–818. [[CrossRef](#)]
16. Kamata, K.; Sugahara, K. Base Catalysis by Mono- and Polyoxometalates. *Catalysts* **2017**, *7*, 345. [[CrossRef](#)]
17. Hayashi, S.; Yamazoe, S.; Koyasu, K.; Tsukuda, T. Lewis Base Catalytic Properties of $[\text{Nb}_{10}\text{O}_{28}]^{6-}$ for CO_2 Fixation to Epoxide: Kinetic and Theoretical Studies. *Chem. Asian J.* **2017**, *12*, 1635–1640. [[CrossRef](#)]
18. Hayashi, S.; Sasaki, N.; Yamazoe, S.; Tsukuda, T. Superior Base Catalysis of Group 5 Hexametallates $[\text{M}_6\text{O}_{19}]^{8-}$ (M = Ta, Nb) over Group 6 Hexametallates $[\text{M}_6\text{O}_{19}]^{2-}$ (M = Mo, W). *J. Phys. Chem. C* **2018**, *122*, 29398–29404. [[CrossRef](#)]
19. Weng, Z.; Ogiwara, N.; Kitao, T.; Kikukawa, Y.; Gao, Y.; Yan, L.; Uchida, S. Incorporating Highly Basic Polyoxometalate Anions Comprising Nb or Ta into Nanoscale Reaction Fields of Porous Ionic Crystals. *Nanoscale* **2021**, *13*, 18451–18457. [[CrossRef](#)]

20. Gutierrez, L.F.; Nope, E.; Rojas, H.A.; Cubillos, J.A.; Sathicq, Á.G.; Romanelli, G.P.; Martínez, J.J. New Application of Decaniobate Salt as Basic Solid in the Synthesis of 4H-Pyrans by Microwave Assisted Multicomponent Reactions. *Res. Chem. Intermed.* **2018**, *44*, 5559–5568. [[CrossRef](#)]
21. Ge, W.; Wang, X.; Zhang, L.; Du, L.; Zhou, Y.; Wang, J. Fully-Occupied Keggin Type Polyoxometalate as Solid Base for Catalyzing CO₂ Cycloaddition and Knoevenagel Condensation. *Catal. Sci. Technol.* **2016**, *6*, 460–467. [[CrossRef](#)]
22. Zhao, S.; Chen, Y.; Song, Y.-F. Tri-Lacunary Polyoxometalates of Na₈H[PW₉O₃₄] as Heterogeneous Lewis Base Catalysts for Knoevenagel Condensation, Cyanosilylation and the Synthesis of Benzoxazole Derivatives. *Appl. Catal. Gen.* **2014**, *475*, 140–146. [[CrossRef](#)]
23. Kikkawa, S.; Tsukada, M.; Shibata, K.; Fujiki, Y.; Shibusawa, K.; Hirayama, J.; Nakatani, N.; Yamamoto, T.; Yamazoe, S. Base Catalysis of Sodium Salts of [Ta_{6-x}Nb_xO₁₉]⁸⁻ Mixed-Oxide Clusters. *Symmetry* **2021**, *13*, 1267. [[CrossRef](#)]
24. Sugahara, K.; Kimura, T.; Kamata, K.; Yamaguchi, K.; Mizuno, N. A Highly Negatively Charged γ -Keggin Germanodecatungstate Efficient for Knoevenagel Condensation. *Chem. Commun.* **2012**, *48*, 8422–8424. [[CrossRef](#)]
25. Chudatemiya, V.; Kikkawa, S.; Hirayama, J.; Takahata, R.; Teranishi, T.; Tamura, M.; Yamazoe, S. Bifunctional Platinum-Incorporated Polyoxoniobate Derived Catalyst for *N*-formylation of Piperidine Using CO₂. *Asian J. Org. Chem.* **2022**, e202200521. [[CrossRef](#)]
26. Asakura, H.; Shishido, T.; Yamazoe, S.; Teramura, K.; Tanaka, T. Structural Analysis of Group V, VI, and VII Metal Compounds by XAFS. *J. Phys. Chem. C* **2011**, *115*, 23653–23663. [[CrossRef](#)]
27. Yamazoe, S.; Hitomi, Y.; Shishido, T.; Tanaka, T. XAFS Study of Tungsten L₁- and L₃-Edges: Structural Analysis of WO₃ Species Loaded on TiO₂ as a Catalyst for Photo-Oxidation of NH₃. *J. Phys. Chem. C* **2008**, *112*, 6869–6879. [[CrossRef](#)]
28. Fukada, M.; Shibata, K.; Imai, T.; Yamazoe, S.; Hosokawa, S.; Wada, T. Fabrication of Lead-Free Piezoelectric NaNbO₃ Ceramics at Low Temperature Using NaNbO₃ Nanoparticles Synthesized by Solvothermal Method. *J. Ceram. Soc. Jpn.* **2013**, *121*, 116–119. [[CrossRef](#)]
29. Asakura, H.; Yamazoe, S.; Misumi, T.; Fujita, A.; Tsukuda, T.; Tanaka, T. xTunes: A New XAS Processing Tool for Detailed and on-the-Fly Analysis. *Radiat. Phys. Chem.* **2020**, *175*, 108270. [[CrossRef](#)]
30. Momma, K.; Izumi, F. VESTA 3 for Three-Dimensional Visualization of Crystal, Volumetric and Morphology Data. *J. Appl. Crystallogr.* **2011**, *44*, 1272–1276. [[CrossRef](#)]

Disclaimer/Publisher's Note: The statements, opinions and data contained in all publications are solely those of the individual author(s) and contributor(s) and not of MDPI and/or the editor(s). MDPI and/or the editor(s) disclaim responsibility for any injury to people or property resulting from any ideas, methods, instructions or products referred to in the content.